

1 **Observationally based analysis of land-atmosphere** 2 **coupling**

3

4 **F. Catalano¹, A. Alessandri¹, M. De Felice¹, Z. Zhu^{2,3} and R. B. Myneni⁴**

5 [1]{Italian National Agency for New Technologies, Energy and Sustainable Economic
6 Development (ENEA), Rome, Italy}

7 [2]{State Key Laboratory of Remote Sensing Science, Institute of Remote Sensing and
8 Digital Earth, Chinese Academy of Sciences, Beijing, China}

9 [3]{Center for Applications of Spatial Information Technologies in Public Health, Beijing,
10 China}

11 [4]{Department of Earth and Environment, Boston University, Boston, MA, USA}

12 Correspondence to: F. Catalano (franco.catalano@enea.it)

13

14 **Abstract**

15 The temporal variance of soil moisture, vegetation and evapotranspiration over land has been
16 recognized to be strongly connected to the temporal variance of precipitation. However, the
17 feedbacks and couplings between these variables are still not well understood and quantified.
18 Furthermore, soil moisture and vegetation processes are associated to a memory and therefore
19 they may have important implications for predictability.

20 In this study we apply a generalized linear method, specifically designed to assess the
21 reciprocal forcing between connected fields, to the latest available observational datasets of
22 global precipitation, evapotranspiration, vegetation and soil moisture content. For the first
23 time a long global observational dataset is used to investigate the spatial and temporal land
24 variability and to characterize the relationships and feedbacks between land and precipitation.

25 The variables considered show a significant coupling among each other. The analysis of the
26 response of precipitation to soil moisture evidences a robust coupling between these two
27 variables. In particular, the first two modes of variability of the precipitation forced by soil
28 moisture appear to have a strong link with volcanic eruptions and ENSO cycles, respectively,

1 and these links are modulated by the effects of evapotranspiration and vegetation. It is
2 suggested that vegetation state and soil moisture provide a biophysical memory of ENSO and
3 major volcanic eruptions, revealed through delayed feedbacks on rainfall patterns. The third
4 mode of variability reveals a trend very similar to the trend of the inter-hemispheric contrast
5 in SST and appears to be connected to greening/browning trends of vegetation over the last
6 three decades.

7

8 **1 Introduction**

9 Soil moisture (SM) is an important variable of the climate system, playing an important role
10 in the feedbacks between land-surface and atmosphere. SM is important in determining
11 climate variability at a wide range of temporal and spatial scales and controls hydrologic and
12 energy cycles (Seneviratne et al., 2010; Dirmeyer, 2011). Soil moisture-precipitation
13 feedbacks have been investigated at the global (Koster et al., 2004; Koster et al., 2009) and
14 the regional (Pal and Eltahir, 2003; Hohenegger et al., 2009) scale through numerical
15 simulations. Recent observational studies focused on local land-atmosphere coupling
16 (Santanello et al., 2009). However, a comprehensive observational study at the global scale of
17 the SM precipitation (PRE) coupling has never been performed. As shown by several
18 modelling studies, it is over transition zones between wet and dry climates that a strong
19 coupling between soil moisture and precipitation can be clearly identified and it is over these
20 regions that “soil moisture memory” can most probably contribute to subseasonal and longer
21 climate predictions (Koster et al., 2004; Ferranti and Viterbo, 2006). The term “soil moisture
22 memory” refers to the property of soil moisture to display persistent anomalies induced by
23 climatic events like ENSO or volcanic eruptions. Since slowly varying states of the land
24 surface can be predicted weeks to months in advance, the response of the atmosphere to these
25 land-surface anomalies can contribute to seasonal prediction. The large discrepancies among
26 model results evidence the need of observational analysis of soil moisture-precipitation
27 feedbacks (Seneviratne et al., 2010). The observational study by Alessandri and Navarra
28 (2008) clearly identified a link between rainfall and land surface-vegetation variability
29 indicating an important delayed feedback of the land surface to the precipitation pattern. In
30 this regard, a mechanism by which vegetation may provide delayed memory of El Niño and
31 La Niña events is identified.

1 Predictability of climate at seasonal and longer time scales stems from the interaction of the
2 atmosphere with slowly varying components of the climate system such as the ocean and the
3 land surface (Shukla and Kinter, 2006). However, much of the model improvements so far
4 have been obtained over ocean, where extensive availability of observations allowed model
5 progresses and reliable application of assimilation techniques (Rosati et al., 1997; Alessandri
6 et al., 2010; Alessandri et al., 2011). In contrast, forecasts performance over land is
7 substantially weaker compared to the ocean (Wang et al., 2009; Alessandri et al., 2011). Since
8 most of the applications of climate predictions would serve economic interests that are land-
9 based, there is an urgent need to improve climate forecasts over land. Long-term
10 improvements in understanding land-climate interactions and feedbacks over land must come
11 from the enhancement of the description of the physical processes on the basis of dedicated
12 process studies and observational databases. This can be suitably pursued firstly by analysing
13 the newest available satellite-derived observational datasets that can lead to a better
14 understanding and quantification of land surface-atmosphere feedbacks. The better knowledge
15 will then help us to conceive improved systems for the simulation of climate and for the
16 improvement of its prediction at seasonal and possibly longer time scales. Here a global array
17 of relevant up-to-date high quality datasets is acquired, harmonized and analysed. The
18 comprehensive dataset is analysed to characterize the seasonal-mean interannual variability of
19 land-surface variables and to improve understanding of the relationship and feedbacks
20 between land and climate. The analysis method is based on the Coupled Manifold (CM)
21 technique (Navarra and Tribbia, 2005) which has been specifically designed to analyse
22 covariation between fields considering both the local and remote forcing of one field to the
23 other. The CM has proved to be successful for the analysis of different climate fields, like
24 precipitation, vegetation characteristics, sea surface temperature, and temperature over land
25 (Alessandri and Navarra, 2008; Cherchi et al., 2007; Wang et al., 2011). Recently, the CM
26 technique has been also applied to investigate the relationship between surface temperature
27 and electricity demand in summer (De Felice et al., 2014). By taking advantage of the new
28 global array of relevant up to date high quality datasets, the present work substantially
29 extends the analysis previously performed by Alessandri and Navarra (2008) and, for the first
30 time, it includes SM and evapotranspiration (ET) feedbacks on PRE.

31 This paper is organized as follows: the observational datasets are described in Section 2.
32 Section 3 describes the analysis method and gives a brief introduction of the CM technique.

1 Section 4 presents the results. Summary and discussion of the main results of this study are
2 given in Section 5.

3

4 **2 The observational datasets**

5 The datasets used for this study are all observationally based, in order to make the analysis as
6 much as possible independent from global circulation model limitations and biases. High
7 quality up-to-date observational datasets of precipitation (PRE, from the Global Precipitation
8 Climatology Project [GPCP]), Evapotranspiration (ET, from University of Montana), soil
9 moisture (SM, from European Space Agency [ESA]) and Leaf Area Index (LAI, from Boston
10 University) have been acquired and prepared. The selection of the datasets is based mainly on
11 two criteria: 1) as long as possible period covered; 2) global spatial coverage. The observed
12 monthly PRE dataset is described in Adler et al. (2003). ET values are satellite-based
13 estimates from the Global Inventory Modeling and Mapping Studies [GIMMS] and MODIS
14 (Zhang et al., 2010). The SM dataset (Liu et al., 2011, 2012) is the most complete record of
15 this variable, based on active and passive microwave satellite sensors. The LAI dataset (Zhu
16 et al., 2013) is a long-term global data set resulting from the application of a neural network
17 algorithm to the NDVI3g product from GIMMS satellite data. All land-surface datasets (SM,
18 ET, LAI) are satellite products independent on the PRE dataset, which is based on rain
19 gauges. Despite both ET and LAI products have been acquired by using the AVHRR sensor,
20 the datasets have been produced by independent research groups which used completely
21 different methodologies. The LAI product has been generated by applying a neural network
22 algorithm on the NDVI satellite product while the ET dataset has been produced by using a
23 modified Penman-Monteith approach including eddy covariance and meteorological data
24 from the FLUXNET towers network. The time period, depending from the availability of the
25 datasets, is 24 years (1983-2006) for ET and 29 years (1982-2010) for the other variables.
26 Original datasets come with various sampling frequencies, ranging from daily to monthly. See
27 Table 1 for a summary of the characteristics of the retrieved datasets.

28 The data have been pre-processed and prepared for the subsequent analysis (Table 1). The
29 pre-processing included space and time averaging, analysis of the spatial coverage and gap
30 filling in order to minimize the effect of undefined values (hereinafter NaN). The gap filling
31 procedure is described in Section 3. ET and PRE datasets are observational products merged
32 with model information and so do not contain NaNs. Instead, LAI and SM are affected by

1 data gaps and present significant seasonal variation of the spatial coverage. Fig. 1a reports the
 2 seasonal cycle of the percentage of NaN values for LAI (full line) and SM (dashed line). Both
 3 variables show better spatial coverage during the summer season (June, July, August,
 4 September). On the other hand, mostly because satellite-based estimates of LAI and SM are
 5 unreliable in presence of snow cover (Zeng et al., 2013), during the winter season the
 6 coverage reduces substantially. The SM dataset derives from blending passive and active
 7 microwave satellite retrievals. Fig. 1b shows the percentage of SM missing data for each grid
 8 point. All grid points with a percentage of missing number larger than 30% (white areas in
 9 Fig. 1b) have not been considered in the analysis. Over regions characterized by particularly
 10 dense vegetation and high canopies, both satellite products are unable to provide reliable
 11 estimates (Liu et al., 2012). Conversely, non-vegetated areas are associated to NaN values in
 12 the LAI dataset.

13 In order to evaluate the effect of major volcanic eruptions on land-atmosphere coupling, we
 14 used the stratospheric Aerosol Optical Depth (AOD) at 550 nm, available from the NASA
 15 GISS dataset (Sato et al., 1993). To evaluate the effect of ENSO, we compute the NINO3
 16 index based on the HadISST 1.1 – Global sea-Ice coverage and Sea Surface Temperature
 17 (1870–present; Rayner et al., 2003) dataset.

18

19 **3 The Analysis Method**

20 The CM technique (Navarra and Tribbia, 2005) seeks linear relations between two
 21 atmospheric fields Z and S (that in general are assumed to be rectangular matrices) of the
 22 kind:

$$23 \quad Z = Z_{for} + Z_{free} = AS + Z_{free}, \quad (1)$$

$$24 \quad S = S_{for} + S_{free} = BZ + S_{free}, \quad (2)$$

25 The subscript $()_{for}$ indicates the component of the field forced by the other variable
 26 (hereinafter forced manifold), while $()_{free}$ indicates the free manifold. The free manifold
 27 contains the effects of nonlinearities. The linear operators A and B express the link between Z
 28 and S . A expresses the effect of S on Z , while B represents the effect of Z on S . In general, A
 29 and B are different. A and B are found by solving the Procrustes minimization problem:

$$30 \quad A = ZS'(SS')^{-1}, \quad (3)$$

1 $B = SZ'(ZZ')^{-1},$ (4)

2 Following Navarra and Tribbia (2005), the technique is applied to the principal components
3 of Z and S, therefore the coefficients of the linear operators A and B express the relations
4 between the modes of the two variables. CCA scaling (data scaled by the covariance matrices)
5 is applied to the Principal Components (PCs) of the variables before solving the Procrustes
6 problem:

7 $\hat{Z} = (ZZ')^{-1/2},$ (5)

8 $\hat{S} = (SS')^{-1/2},$ (6)

9 where \hat{Z} and \hat{S} are the CCA-scaled variables. Please refer to Navarra and Tribbia (2005) for
10 further details of the CM technique.

11 As explained in Cherchi et al. (2007), after applying the CCA scaling, the elements of A and
12 B are correlation coefficients and can be tested (with a significance test based on the Student t
13 distribution) to reject the null hypothesis of being equal to zero. To improve the robustness of
14 the analysis, each element of the A and B matrices has been verified to be different from zero
15 at the 1% significance level, following the method proposed by Cherchi et al. (2007).

16 The CM has two main advantages compared to other methods. The first one is that, when
17 applied to a couple of climate fields (i.e., PRE and SM), CM is able to separate one field (i.e.,
18 PRE) into two components: the first component (forced) is the portion of PRE variability that
19 is connected to the SM variability, whereas the second (free) is the part of PRE that is
20 independent from SM. Therefore, the CM technique enables to find robust relations between
21 fields in the presence of strong background noise. The second advantage is that the CM
22 technique is able to detect both local and remote effects of the forcing variable. This is not
23 possible with other methods such as SVD (Singular Value Decomposition).

24 In the present analysis the CM technique has been applied to the seasonal-mean inter-annual
25 anomalies. The climatological seasonal cycle has been removed and the data have been
26 stratified using the seasons: JFM (January-February-March), AMJ (April-May-June), JAS
27 (July-August-September) and OND (October-November-December). The JFM, AMJ, JAS,
28 OND stratification has been used by Alessandri and Navarra (2008) in their CM study of
29 vegetation and rainfall which we will use to compare our results. The trends are kept for their
30 relevance as possible indicators of climate change.

1 The LAI and SM datasets contain missing values, whose number and position significantly
2 vary with time. The application of the CM algorithms requires that the number and position of
3 the missing values is constant with time. Hence, if a NaN is present in a given grid-point at
4 any time, then it requires to mark as NaN that grid point, thus losing a great amount of
5 information. In order to keep as much information as possible from the data, we decided to
6 replace the missing values with climatological values provided that their total number,
7 considering a particular grid-point, does not exceed a given threshold. We selected different
8 thresholds for SM and LAI in order to obtain as similar as possible spatial coverage of the two
9 variables. The chosen threshold is 10% for LAI and 30% for SM. The results are robust with
10 respect to a $\pm 10\%$ change of the threshold values. As shown in Fig. 1b, the areas more
11 affected by the replacement of SM missing values (30% of values replaced by climatology)
12 are North-East Europe, East coast of Central-South America, East China and Korea. Since the
13 replacement of missing values with climatology reduces time variability, the coupling in these
14 regions may be underestimated as a consequence. We note that these gap-filled regions do not
15 correspond to transition zones between wet and dry climates (Koster et al., 2000). Therefore,
16 they are not expected to display a strong coupling between SM and PRE and to significantly
17 affect the main results of present study.

18 Since the main interest of the work is on the land-surface, the ocean values are masked out
19 from the PRE dataset. A preliminary analysis (not shown) revealed that their inclusion
20 resulted in a more difficult interpretation of the Empirical Orthogonal Functions (EOF)
21 patterns (Bretherton et al., 1992), due to the interaction of phenomena on different space and
22 time scales which are not connected to land variables.

23

24 **4 Results**

25 The CM technique has been applied to analyse the reciprocal forcing between PRE and the
26 observed surface variables (SM, ET, LAI). The global-scale reciprocally forced temporal
27 variances between PRE and the land surface variables is reported in Table 2. 19% of the PRE
28 variability is forced by SM. On the other hand, 17% of the SM variance appears to be forced
29 by PRE. 18% of the variability of PRE is forced by ET and 14% of the variance of ET is
30 forced by PRE. Considering the coupling between PRE and LAI, 17% of the variance of PRE
31 appears to be forced by LAI and 14% of the variability of LAI is forced by PRE. All the
32 variance ratios in Table 2 are significant at the 1% level. The chance of coincidentally getting

1 as high or higher ratios has been tested by means of a Monte Carlo bootstrap method (1000
2 repetitions).

3 Since SM is the most important land-surface parameter affecting seasonal to interannual
4 variability/predictability of precipitation (Koster et al., 2000; Zhang et al., 2008), the coupling
5 between SM and PRE will be analyzed in detail in the following.

6 **4.1 Reciprocal forcing between PRE and SM seasonal-mean anomalies**

7 Fig. 2 shows the ratio of the forced/total variance over land. The ratio of SM variance forced
8 by PRE is in panel a, while panel b shows the ratio of PRE variability which is accounted for
9 by the SM variability. For each grid point, the null hypothesis of coincidentally getting as
10 high or higher variance ratios has been tested using a Monte Carlo bootstrap method (1000
11 repetitions). The regions where the ratio values are not significantly different from zero at the
12 1% level are dotted. The observed SM variability appears to be intensely forced by PRE over
13 the Sahel and Central-eastern Africa, South Africa, Middle East, the semi-arid region of
14 Central West Asia, Indian Peninsula, Argentina, Eastern Brazil and Australia. Note that, due
15 to the limitations of the satellite estimates discussed in Section 2, large areas in Russia and the
16 Amazon basin are not covered in the SM dataset. The larger observed effects on PRE due to
17 SM inter-annual variability (Fig. 2b) occur in East Brazil, La Plata basin, Sahel, Asian boreal
18 forests, Middle East, Pakistan, Indonesia, northern and eastern Australia. Most of these
19 regions correspond to transition zones between dry and wet climates, where evaporation is
20 highly sensitive to soil moisture (Koster et al., 2000). Here we refer to the transition regions
21 between very dry and very humid environments, as individuated by Koster et al. (2000).

22 By using the CM technique (described in Section 3), the seasonal-mean PRE anomalies are
23 separated into forced and free components, where forced and free refers to the influence of the
24 SM variation. The variance explained by each mode of the PRE forced field is reported in
25 Table 3. The EOF analysis shows that the first three components of the variability of the
26 forced PRE field together account for 48% of total variance. The first two PCs does not
27 display trends while the third PC is dominated by a clear trend, as will be discussed later. The
28 first mode of variability of the forced PRE field explains 26% of the total variance. The
29 corresponding principal component displays two significant peaks at years 1983 and 1992
30 (Fig. 3a). The PC is significantly correlated (maximum correlation coefficient equal to 0.56 at
31 lag 0) to the stratospheric AOD. AOD peaks in correspondence of the two major eruptions of

1 the period: 1983 (El Chichon) and 1992 (Pinatubo). The peaks in the AOD time series
2 correspond to those of the forced PRE PC1, suggesting that this mode of variability is related
3 to changes in the solar radiation at the ground, confirming that absorption and reflection of
4 solar radiation by aerosol are particularly effective in reducing the hydrological cycle. The
5 fast response of the precipitation anomalies to the radiation change induced by large tropical
6 volcanic eruptions is in agreement with the results of the lag-correlation analysis by Gu and
7 Adler (2011), who found 0 time lag between stratospheric aerosol signal and PRE. The lagged
8 correlations of PC1 and AOD (Fig. 3b) show that significant (at 5% level) correlations endure
9 up to about 2 years after the aerosol peak (i.e: behind the autocorrelation period of AOD
10 itself; Fig. 3b dashed line). This result indicates that SM may provide a memory of the major
11 volcanic eruptions for PRE. Table 4 shows the variance explained by each EOF mode of the
12 whole original PRE field (that is, forced+free components). The link between PRE and
13 volcanic eruption signal is evident also in the first mode of variability of the total rainfall field
14 as confirmed by the correlation of the corresponding PC (explaining 10% of total PRE
15 variance) with AOD (Table 4).

16 Fig. 3c shows the spatial pattern of the first EOF of the PRE anomalies forced by the SM. A
17 clear negative signal is present over areas characterized by a wet climate (Amazon basin,
18 India and Indonesia). In these regions the stratospheric aerosol emitted during the volcanic
19 eruptions has the effect of reducing the intensity of the hydrological cycle (Alessandri et al.,
20 2012) with a consequent reduction of SM, PRE and continental discharge (Trenberth and Dai,
21 2007). In particular, according to Joseph and Zeng (2011) and Iles et al. (2013), the negative
22 signal over the monsoon regions may indicate a suppression of the monsoon linked to the
23 effects of the aerosol released during major eruptions. Further, differently from our results
24 and other observational (Trenberth and Dai, 2007) and modelling (Joseph and Zeng, 2011)
25 studies, the HadCM3 results of Iles et al. (2013) showed a wetting signal over India during the
26 summer season (although not significant in the observational dataset they used). On the other
27 hand, over transition zones (U.S. Great Plains, Argentina, Middle East) the dimming effect
28 may result in reduced evapotranspiration during the hot/dry season which drives an increase
29 of SM (Wild et al., 2009). During the following cool/wet season, the enhanced SM can induce
30 a lagged increase of the portion of PRE forced by SM. That can explain the increased PRE
31 over transition areas. On the other hand, the reduction of PRE over South Asia monsoon
32 region and the enhancement of PRE over the semi-arid areas of Central West Asia is
33 consistent with the monsoon-desert mechanism (Rodwell and Hoskins, 1996; Cherchi et al.,

1 2014): the reduction of radiation caused by the stratospheric aerosol drives a reduction of
2 convection over monsoon regions and a consequent reduction of PRE over South Asia
3 therefore abating Rossby wave induced subsidence over Middle East and East Mediterranean
4 (Cherchi et al., 2014).

5 The second PC of PRE forced by SM, explaining 14% of total variance, is dominated by a
6 large scale oscillation (Fig. 4a). The corresponding principal component (full line) displays an
7 high correlation coefficient of 0.60 with the NINO3 index (average of the Sea Surface
8 Temperature in the tropical Pacific region 5S–5N, 210–270E; dashed line) at lag 2 (significant
9 at the 1% level), indicating that EOF2 represents the portion of the rainfall forced by SM that
10 is related to the El Niño Southern Oscillation (ENSO; Philander, 1989) variability. The
11 second mode of forced PRE response due to SM variability appears to be lagged by one to
12 several seasons with respect to the ENSO phase (Fig. 4b), with the strongest correlations with
13 the NINO3 index two seasons after the maximum El Niño or La Niña intensity and significant
14 correlations enduring until the lag 5 season (i.e: behind the autocorrelation period of ENSO
15 itself; Fig. 5b dashed line). The results indicate that the effects related to ENSO in the SM
16 may induce a delayed forcing on PRE. Therefore, SM appears to provide a biophysical
17 memory of ENSO on the global precipitation pattern. The signal of ENSO can also be
18 evidenced in the second mode of variability of the total rainfall field as indicated by the
19 correlation of the corresponding PC (explaining 5% of total PRE variance) with NINO3
20 (Table 4). Again, the lag at which maximum correlation is attained is the same (lag 2) as in
21 the forced field but the correlation coefficient is 0.60 for the forced field and 0.43 for the total
22 PRE field.

23 The spatial pattern of the second EOF of the PRE anomalies forced by SM (Fig. 4c) displays
24 the signature of the tripole pattern over south America typical of ENSO teleconnections
25 (Ropelewski and Halpert, 1989). Similarly, negative PRE anomalies are shown over Brazil,
26 South Africa, North India and Indochina, displaying the land surface feedback to the reduced
27 rainfall related to the positive phase of ENSO there (Trenberth et al., 1998). On the other
28 hand, positive precipitation anomalies characterize the West and East Coasts of North
29 America, Central America, the dry and semi-arid region of North Venezuela, La Plata basin,
30 Horn of Africa, Sahel, Europe, Central and East Asia, South India and the East Coast of
31 Australia. Most previous research showed reduced precipitation over India during ENSO
32 years (Ropelewski and Halpert, 1989; Trenberth et al., 1998). The positive anomalies of PRE

1 forced by SM over South India related to the positive phase of ENSO evidence an interesting
2 negative feedback of the land-surface on the effect of ENSO on the rainfall over India.

3 The third PC of the PRE forced by the SM, explaining 8% of forced variance, displays a trend
4 (Fig. 5a) corresponding to a clear signal of increasing precipitation over the Sahel, South-East
5 Europe, Central Asia, North-East Asia, the Great Plains of North America, Nordeste and the
6 Northern part of South America (Fig. 5b). The trend of increasing precipitation is particularly
7 strong over the Sahel where, according to Hagos and Cook (2008), it can be related to a
8 warming of the northern tropical Atlantic Ocean which, through a modification of the
9 associated cyclonic circulation, enhances moisture transport over the region. In contrast, a
10 decrease of precipitation is evident over most of the Southern Hemisphere (SH), North West
11 Russia, East Russia, North India, China and West US, showing a north-south polarity of the
12 precipitation trend. The above trend pattern strongly resembles the trend pattern of global
13 rainfall annual mean anomalies described by Munemoto and Tachibana (2012, hereinafter
14 MT12). The authors associated this North-South polarity to a relatively larger warming of the
15 Northern Hemisphere (NH) compared to the SH that characterized the last three decades
16 starting from the early 1980s. MT12 found that the trend of the SST corresponds to an
17 increase of the specific humidity in the NH with respect to SH that enhances (reduces)
18 precipitation in the NH (SH). Although the focus of MT12 is on the Sahel region, the authors
19 defined a global index, the North South SST (NS-SST) polarity index, which successfully
20 captures the global signal of the precipitation trend. The NS-SST index is defined as the area
21 averaged NH SST annual mean anomalies minus the SH SST anomalies. The NS-SST index
22 (computed from HadISST), normalized by its standard deviation, and its trend are plotted in
23 Fig. 5a. Note that here the NS-SST index is computed from the seasonal mean anomalies
24 instead of the annual mean anomalies used in MT12, nonetheless the trend is not affected.

25 **4.2 Mediation effects of ET and LAI on the coupling between PRE and SM**

26 To investigate how the coupling between rainfall and soil moisture is mediated by
27 evapotranspiration and vegetation we further applied the CM technique between the
28 component of PRE forced by SM and ET (LAI), obtaining the component of PRE forced by
29 SM which is also forced by ET (LAI). As summarized in Table 5, 20% of the inter-annual
30 variability of the PRE anomalies forced by the SM is estimated to be globally forced by the
31 ET variation. It is important to note here that $19\% \times 20\% = 3.8\%$ represents only the ET forcing
32 on PRE mediated by SM and not the whole ET forcing on PRE which is actually 18% (Table

1 2). At the same time, 23% of the variance of PRE forced by SM is evaluated to be also forced
2 by LAI, therefore the LAI forcing on PRE mediated by SM corresponds to $17\% \times 23\% = 3.9\%$.

3 Fig. 6a shows the ratio of the variance of PRE forced by the SM which is also forced by the
4 ET with respect to the total forced rainfall variance. Fig. 6b shows the same plot but for the
5 LAI. The “hotspots” in Fig. 6a are similar to those found in Fig. 2b over Sahel, Horn of
6 Africa, East Europe, Asian boreal forests, Central Asia, West Coast of the US, East Brazil and
7 La Plata basin. This indicates that in all these regions the link between PRE and SM is at least
8 in part mediated by ET. Not surprisingly, the same regions also display a link with vegetation
9 (Fig. 6b). Furthermore, vegetation appears to significantly affect rainfall variability over the
10 semi-arid regions that are not dependent on ET such as Central West Asia, South-East Africa,
11 South-East Asia and West Australia, suggesting that in these regions the SM forcing on PRE
12 is mediated by vegetation state (e.g. stress of vegetation will affect PRE there).

13 To analyse how the response of PRE forced by SM to climate events and the trend are
14 mediated by ET (LAI), we applied the CM technique between each of the physical fields
15 corresponding to the first three modes of variability of PRE forced by the SM and ET (LAI).
16 Here we take the physical fields corresponding to the first three modes of variability of PRE
17 forced by SM and further decompose them to extract the parts of each mode that is forced by
18 ET and LAI, respectively. This analysis allows to figure out how ET and LAI contribute to
19 each component of PRE forced by SM which has been identified to be linked to external
20 climate forcing (volcanic eruptions, ENSO and trend). Overall, considering the global land,
21 21% of the variance displayed by the first mode (linked to volcanic eruptions) of PRE forced
22 by the SM is forced by the ET and 27% by LAI (Table 6). As for the second mode (connected
23 to ENSO), 38% of the variance is forced by ET and 36% by LAI. Concerning the third mode
24 (displaying a trend), 31% of the variance is forced by ET and 29% is forced by LAI. Rainfall
25 variability forced by the ET and LAI decomposed through EOF analysis is reported in Table
26 7. Interestingly, the third PC of the PRE forced by the ET (explaining 7% of the forced
27 variance) is correlated with AOD, with a maximum correlation coefficient of 0.41 at lag 6.
28 Analogously, the second PC of the PRE anomalies forced by the LAI (explaining 10% of the
29 forced variance) is correlated with AOD, with a maximum correlation coefficient of 0.41 at
30 lag 3, suggesting that both ET and vegetation contribute to provide memory of volcanic
31 eruptions, modulating at longer scales the effect of the SM forcing on PRE. The first PC of
32 PRE forced by ET (explaining 30% of the forced variance) is found to be significantly

1 correlated with the NINO3 index with a correlation coefficient of 0.52 at lag 0. The first PC
2 of PRE forced by LAI (explaining 27% of the forced variance) also has a maximum
3 correlation coefficient of 0.67 at lag 0 with the NINO3 index, indicating that vegetation acts
4 as the mediator at longer scales of the signal between SM and PRE. This result is consistent
5 with the relationship found by Alessandri and Navarra (2008) between precipitation forced by
6 vegetation (NDVI) and ENSO and with the delayed vegetation response to ENSO signal
7 found by Zeng et al. (2005). All the above correlation coefficients passed a significance test at
8 1% level.

9 To determine the regions where the mediating effects of ET and LAI have the larger influence
10 on the coupling with respect to the stratospheric volcanic eruptions, the first mode of
11 variability of PRE forced by the SM has been correlated with the total components of PRE
12 forced by the ET and LAI. The correlation coefficients are shown in Fig. 7a for PRE forced
13 by the ET and Fig. 7b for PRE forced by the LAI. Only the regions where correlations passed
14 a significance test at 5% level are shaded. Black upward (white downward) triangles denote
15 areas with positive (negative) values of the first EOF of the PRE anomalies forced by the SM
16 (Fig. 3c). The correlations are positive almost everywhere (i.e. the effects of both ET and LAI
17 tend to amplify the response of rainfall to large volcanic eruptions) and the patterns are very
18 similar for ET and LAI, indicating that the feedback of ET may be linked to the stress of
19 vegetation consequent to the effect of volcanic eruptions on radiative forcing. Large values
20 (up to 0.6) are seen over Central US, North West Brazil, La Plata basin, West Central Asia,
21 Horn of Africa, South Africa, the Asian monsoon region, Indonesia and Australia. Over these
22 regions evapotranspiration and vegetation activity are radiation limited (Seneviratne et al.,
23 2010). Nevertheless, while over some regions (Southern part of North America, La Plata
24 basin, Middle East, West Central Asia and Horn of Africa) ET and LAI contribute to an
25 increase of rainfall, over other regions (Northern South America, South Africa, Indian
26 monsoon region, Australia) they contribute to rainfall reduction. As discussed in Section 4.1,
27 over most of the SH (apart from La Plata basin and Horn of Africa) and the Asian monsoon
28 region there is a reduction of precipitation that can be associated to the dimming effect and
29 the consequent reduction of the hydrological cycle. In humid regions the rainfall reduction
30 can stress vegetation and may reduce its growth with effects lasting up to one year (Wang et
31 al., 2011b). On the other hand, over most of the arid and semi-arid regions (Middle East, West
32 Central Asia), the reduced evapotranspiration during past seasons induced by the dimming

1 effect may increase SM and therefore attenuate the stress on vegetation. This, in turn, has a
2 positive effect on precipitation.

3 The point-by-point correlation coefficient between the second mode of variability (related to
4 ENSO) of PRE forced by the SM and the total fields of PRE forced by the ET and PRE forced
5 by the LAI is shown in Fig. 8 on panel a and b, respectively. The sign of the feedback
6 between PRE and SM is indicated by the second EOF of PRE forced by the SM overlaid to
7 the plot. Large positive correlations up to 0.6 are found globally over most of the land areas.
8 ET has a positive feedback on the increase of precipitation over the West Coast of US, the dry
9 and semi-arid region of North Venezuela, La Plata basin, Sahel, North Europe, India, Central
10 and East Asia and the South-East Coast of Australia. Still a positive feedback is present over
11 Brazil, South Africa and Indochina but in this case ET leads to further reduction of PRE. A
12 negative feedback of ET is seen over Mexico. In this region the positive ENSO phase induces
13 wet and cool conditions (Trenberth et al., 1998) associated to an increase of PRE forced by
14 SM that is contrasted by a reduction of ET. As for vegetation, it contributes to rainfall
15 enhancement over East and West Coasts of the US, La Plata basin, North Europe, Horn of
16 Africa, the semi-arid region of West Central Asia and East Asia. Conversely, vegetation
17 mediates precipitation reduction over Brazil, South Africa and Indochina.

18 Fig. 9 shows the point-by-point correlation coefficient between the third mode of variability
19 of PRE forced by the SM (displaying a linear trend, see Fig. 5) and the total fields of PRE
20 forced by the ET (Fig. 9a) and PRE forced by the LAI (Fig. 9b) with the third EOF of PRE
21 forced by the SM overlaid on it. The feedback of ET on this mode of variability of PRE is not
22 significant over most of the NH. A positive effect of ET is seen over the semi-arid regions of
23 the SH but while over Sahel ET mediates an increase of rainfall, over Bolivia and Australia
24 ET leads to further reduction of PRE (Fig. 9a). On the other hand, ET has a negative feedback
25 over the humid region of Tanzania where it contrasts the reduction of PRE. The pattern of the
26 feedback of LAI (Fig. 9b) is very different from that of ET. Overall, the vegetation has a
27 positive feedback on the rainfall anomaly pattern forced by the SM. In particular, large
28 correlations up to 0.6 are seen over the Sahel, East Coast of the US, West South America,
29 East Europe, Tropical South Africa, West Central Asia, Asian boreal forests, Central and East
30 Asia, the Indian monsoon region and East Australia. The strong signal over the Sahel is in
31 agreement with Zeng et al. (1999) and Kucharski et al. (2013) who found that vegetation
32 feedback amplifies rainfall response to the SST variations on the decadal scale. LAI mediates

1 rainfall enhancement over the Sahel, East Coast of the US, Europe, the semi-arid region of
2 West Central Asia and the Indian monsoon region. Conversely, vegetation contributes to a
3 reduction of PRE over most of the SH (in particular over South America, South Africa and
4 East Australia), the West Coast of the US and East Asia. Fig. 9c shows the linear vegetation
5 trend over the period 1982-2010. Only areas where trend passed a significance test at the 5%
6 level are shown. Significant positive (greening) trend is seen in large parts of the NH (the East
7 Coast of the US, Sahel, Europe, West Central Asia, India and Asian boreal forests). A
8 negative vegetation trend (browning) appears over the West Coast of the US, West South
9 America, the tropical region of South Africa and East Asia. The greening/browning trends in
10 Fig. 9c are consistent with those found by de Jong et al. (2013). A comparison of panels b and
11 c of Fig. 9 evidences that most of the areas characterized by a positive trend of rainfall
12 anomalies are associated to a greening trend of vegetation while areas displaying a decrease
13 of PRE are regions associated to a browning trend. Therefore, the response of rainfall
14 anomalies forced by the SM to the inter-hemispheric SST trend appears to be coupled to a
15 greening/browning trend of vegetation activity. Furthermore, the third PC of PRE forced by
16 LAI displays a trend similar to that of the NS-SST index, analogously to the third PC of PRE
17 forced by SM, while no trends are found in the first five PCs of PRE forced by ET.

18

19 **5 Conclusions**

20 A global array of relevant up-to-date high quality datasets (soil moisture, evapotranspiration,
21 leaf area index and precipitation) is acquired, harmonized and analysed. For the first time a
22 long comprehensive global observational dataset is used to characterize the land variability as
23 a function of the space and time scales and to improve understanding of the relationships and
24 feedbacks between land and climate. By applying the Coupled Manifold technique on the
25 seasonal-mean inter-annual anomalies, the relationship and the coupling between the acquired
26 surface variables is assessed considering all the seasons.

27 The analysis shows a considerable degree of reciprocal forcing and coupling in the land
28 surface variables considered. The reciprocal forcing with precipitation is particularly strong
29 for the soil moisture, with 19% of the inter-annual variability of the precipitation over
30 continental areas that are forced by the SM variation. Conversely, 17% of the SM variance is
31 forced by PRE.

1 The PRE forced by the SM is dominated by a prominent decadal-scale drying, initiated by the
2 perturbation of the abrupt Mt. Pinatubo eruption. In 1991, the PC1 of the dominant forced
3 mode of PRE shows an abrupt decrease and the negative anomaly continues increasing in the
4 subsequent years until 1994. It is only after 1995 that the rainfall starts to slowly recover
5 towards the pre-eruption levels. In 1997, the signal sums-up with that of ENSO. It appears
6 that the persistence of the negative SM anomalies leads to increasing stress conditions for the
7 vegetation, thus leading to a larger ET response at longer time-lags after the perturbing event.
8 Our interpretation is that the persistence of the negative SM anomalies provides the memory
9 of the initial perturbing event and our analysis indicate that, through this mechanism, the
10 effect of Mt. Pinatubo eruption can last for several years and its memory appears to extend
11 and sum to the following 1997-1998 El Niño event. The second PC of the PRE forced by the
12 SM displays a large-scale oscillation correlated to ENSO variability with significant
13 correlations enduring behind the autocorrelation period of ENSO itself and up to more than
14 one year lag. This indicates that ENSO effects on SM induce a delayed forcing on PRE. The
15 third PC of the PRE forced by the SM is dominated by a trend, positive over most of the NH
16 and negative over most of the SH. This trend appears to be related to the inter-hemispheric
17 SST contrast to which corresponds an increase of the specific humidity in the NH with respect
18 to the SH that enhances (reduces) precipitation and SM in the NH (SH).

19 The combined analysis of the PRE modes related to the external climate forcings (volcanic
20 eruptions, ENSO, SST trend) and the rainfall forced by ET and LAI evidences the role of ET
21 and LAI as the mediators between SM forcing and rainfall. In particular, it appears that both
22 ET and LAI tend to provide a positive feedback on PRE over most of the regions,
23 contributing to further enhance or reduce rainfall depending on the regions of the globe, with
24 large differences between wet, transition and semi-arid climates. Nevertheless, the response to
25 ENSO is characterized by a negative feedback of ET over regions where the positive ENSO
26 phase induces wet and cool conditions (i.e. Mexico).

27 It is important to note that the coupling with SM revealed by the present analysis has to be
28 considered an underestimation of the real coupling, due to the incomplete cover of the SM
29 dataset. Nevertheless, the present investigation identifies the regions characterized by a strong
30 coupling and suggests most possible mechanisms linking the considered variables.

31 Since SM has been recognized as the most important land-surface parameter affecting
32 seasonal to interannual variability of precipitation (Koster et al., 2000; Zhang et al., 2008) the

1 present paper focused on the coupling between SM and PRE. Detailed analysis of the
2 reciprocal forcing between ET and LAI, LAI and SM and ET and SM will be the subject a
3 future paper that will further address the specific coupling among land-surface variables.

4

5 **Data availability**

6 Evapotranspiration dataset available from the Numerical Terradynamic Simulation Group
7 (NTSG) of the University of Montana. Web: <http://www.ntsug.umt.edu/project/et>

8 Leaf Area Index dataset available from the Department of Earth & Environment of Boston
9 University. Web: <http://sites.bu.edu/cliveg/datacodes/>

10 Soil Moisture dataset available from the European Space Agency (ESA) Climate Change
11 Initiative (CCI). Web: <http://www.esa-soilmoisture-cci.org/>

12 Precipitation dataset available from the Global Precipitation Climatology Project (GPCP).
13 Web: <http://precip.gsfc.nasa.gov/>

14 Aerosol Optical Depth dataset available from the National Aeronautics and Space
15 Administration (NASA) Goddard Institute for Space Studies (GISS). Web:
16 <http://data.giss.nasa.gov/modelforce/strataer/>

17 Sea Surface Temperature dataset available from the Hadley Centre for Climate Prediction and
18 Research (2006): Met Office HadISST 1.1 (Global sea-Ice coverage and Sea Surface
19 Temperature). Web: <http://catalogue.ceda.ac.uk/uuid/facafa2ae494597166217a9121a62d3c>

20

21 **Acknowledgements**

22 The research leading to these results has received funding from the European Union Seventh
23 Framework Programme (FP7/2007- 2013) under SPECS project (grant agreement n° 308378)
24 and by the LIFE10 ENV/FR/208 project FO3REST. We are grateful to the two anonymous
25 reviewers whose comments greatly improved the quality of the manuscript.

26

1 **References**

- 2 Adler, R. F., and Coauthors: The Version-2 Global Precipitation Climatology Project (GPCP)
3 Monthly Precipitation Analysis (1979–Present), *J. Hydrometeorol.*, 4, 1147-1167, 2003.
- 4 Alessandri, A., and Navarra, A.: On the coupling between vegetation and rainfall inter-annual
5 anomalies: Possible contributions to seasonal rainfall predictability over land areas, *Geophys.*
6 *Res. Lett.*, 35, L02718., 2008.
- 7 Alessandri, A., and Coauthors: The INGV-CMCC Seasonal Prediction System: Improved
8 Ocean Initial Conditions *Mon. Weather Rev.* 138 (7), 2930-2952, 2010.
- 9 Alessandri, A., Borrelli, A., Navarra, A., Arribas, A., Déqué, M., Rogel, P., and Weisheimer,
10 A.: Evaluation of probabilistic quality and value of the ENSEMBLES multi-model seasonal
11 forecasts: comparison with DEMETER. *Mon. Weather Rev.*, 139 (2), 581-607,
12 doi:10.1175/2010MWR3417.1, 2011.
- 13 Alessandri, A., Fogli, P. G., Vichi, M., and Zeng, N.: Strengthening of the hydrological cycle
14 in future scenarios: atmospheric energy and water balance perspective. *Earth Syst. Dynam.* 3,
15 199-212, 2012.
- 16 Bretherton, C. S., Smith, C., and Wallace, J. M.: An intercomparison of methods for finding
17 coupled patterns in climate data. *J. Climate*, 5, 541-560, 1992.
- 18 Cherchi, A., Gualdi, S., Behera, S., Luo, J. J., Masson, S., Yamagata, T., and Navarra, A.: The
19 influence of tropical indian ocean SST on the indian summer monsoon, *J. Clim.*, 20, 3083-
20 3105, 2007.
- 21 Cherchi, A., Annamalai, H., Masina, S., and Navarra, A.: South Asian Summer Monsoon and
22 the Eastern Mediterranean Climate: The Monsoon–Desert Mechanism in CMIP5 Simulations,
23 *J. Clim.*, 27, 6877-6903, 2014.
- 24 De Felice, M., Alessandri, A., and Catalano, F.: Seasonal climate forecasts for medium-term
25 electricity demand forecasting, *Appl. Energy*, 137, 435-444, 2014.
- 26 de Jong, R., Verbesselt, J., Zeileis, A., and Schaepman, M. E.: Shifts in Global Vegetation
27 Activity Trends, *Remote Sens.*, 5, 1117-1133, 2013.
- 28 Dirmeyer, P. A.: The terrestrial segment of soil moisture–climate coupling, *Geophys. Res.*
29 *Lett.*, 38, L16702., 2011.

1 Ferranti, L., and Viterbo, P.: The European summer of 2003: Sensitivity to soil water initial
2 conditions, *J. Clim.*, 19, 3659–3680, 2006.

3 Gu, G., and Adler, R. F.: Precipitation and Temperature Variations on the Interannual Time
4 Scale: Assessing the Impact of ENSO and Volcanic Eruptions, *J. Clim.*, 24, 2258–2270, 2011.

5 Hagos, S. M., and Cook, K. H.: Ocean Warming and Late-Twentieth-Century Sahel Drought
6 and Recovery, *J. Clim.*, 21, 3797–3814, 2008.

7 Hohenegger, C., Brockhaus, P., Bretherton, C. S., and Schar, C.: The Soil Moisture–
8 Precipitation Feedback in Simulations with Explicit and Parameterized Convection, *J. Clim.*,
9 22, 5003–5020, 2009.

10 Iles, C. E., Hegerl, G. C., Schurer, A. P., and Zhang, X.: The effect of volcanic eruptions on
11 global precipitation, *J. Geophys. Res. Atmos.*, 118, 8770–8786, doi:10.1002/jgrd.50678,
12 2013.

13 Joseph, R., and Zeng, N.: Seasonally modulated tropical drought induced by volcanic aerosol,
14 *J. Clim.*, 24(8), 2,045–2,060, doi:10.1175/2009JCLI3170.1, 2011.

15 Koster, R. D., Suarez, M. J., and Heiser, M.: Variance and predictability of precipitation at
16 seasonal-to-interannual timescales, *J. Hydrometeor.*, 1, 26-46, 2000.

17 Koster, R. D., and Coauthors: Regions of Strong Coupling Between Soil Moisture and
18 Precipitation. *Science*, 305, 338-340, 2004.

19 Koster, R. D., Guo, Z., Yang, R., Dirmeyer, P. A., Mitchell, K., and Puma, M. J.: On the
20 Nature of Soil Moisture in Land Surface Models, *J. Clim.*, 22, 4322-4335, 2009.

21 Kucharski, F., Zeng, N, and Kalnay, E.: A further assessment of vegetation feedback on
22 decadal Sahel rainfall variability, *Climate Dyn.*, 40, 1453-1466, DOI:10.1007/s00382-012-
23 1397-x, 2013.

24 Liu, Y. Y., Parinussa, R. M., Dorigo, W. A., De Jeu, R. A. M., Wagner, W., van Dijk, A. I. J.
25 M., McCabe, M. F., and Evans, J. P.: Developing an improved soil moisture dataset by
26 blending passive and active microwave satellite based retrievals. *Hydrology and Earth System
27 Sciences*, 15, 425–436, 2011.

28 Liu, Y. Y., Dorigo, W. A., Parinussa, R. M., De Jeu, R. A. M., Wagner, W., McCabe, M. F.,
29 Evans, J. P., van Dijk, A. I. J. M.: Trend-preserving blending of passive and active microwave
30 soil moisture retrievals. *Remote Sens. Env.*, 123, 280–297, 2012.

- 1 Navarra, A., and Tribbia, J.: The coupled manifold, *J. Atmos. Sci.*, 62, 310-330, 2005.
- 2 Pal, J. S., and Eltahir, E. A. B.: A feedback mechanism between soil-moisture distribution and
3 storm tracks, *Q. J. R. Meteorol. Soc.*, 129, 2279-2297, 2003.
- 4 Philander, S.G.H.: *El Niño, La Niña and the Southern Oscillation*. Academic Press, New
5 York, 293 pp, 1989.
- 6 Rayner, N. A., Parker, D. E., Horton, E. B., Folland, C. K., Alexander, L. V., Rowell, D. P.,
7 Kent, E. C., and Kaplan, A.: Global analyses of sea surface temperature, sea ice, and night
8 marine air temperature since the late nineteenth century, *J. Geophys. Res.*, Vol. 108, No. D14,
9 4407 10.1029/2002JD002670, 2003.
- 10 Rodwell, M. J., and Hoskins, B. J.: Monsoons and the dynamics of deserts, *Q. J. R. Meteorol.*
11 *Soc.*, 122, 1385-1404, 1996.
- 12 Ropelewski, C. F., and Halpert, M. S.: Precipitation Patterns Associated with the High Index
13 Phase of the Southern Oscillation, *J. Clim.*, 2, 268–284, 1989.
- 14 Rosati, A., Miyakoda, K., and Gudgel, R.: The impact of ocean initial conditions on ENSO
15 forecasting with a coupled model. *Mon. Wea. Rev.*, 125, 754–772, 1997.
- 16 Santanello, J. A., Peters-Lidard, C. D., Kumar, S. V., Alonge, C., and Tao, W.-K.: A
17 Modeling and Observational Framework for Diagnosing Local Land-Atmosphere Coupling
18 on Diurnal Time Scales, *J. Hydrometeor.*, 10, 577-599, 2009.
- 19 Sato, M., Hansen, J. E., McCormick, M. P., and Pollack, J. B.: Stratospheric aerosol optical
20 depth, 1850-1990. *J. Geophys. Res.* 98, 22987-22994, 1993.
- 21 Self, S., Rampino, M. R, Zhao, J., and Katz, M. G.: Volcanic aerosol perturbations and strong
22 El Nino events: No general correlation. *Geophys. Res. Lett.*, 24, 1247–1250, 1997.
- 23 Seneviratne, S. I., Corti, T., Davin, E. L., Hirschi, M, Jaeger, E. B., Lehner, I., Orlowsky, B.,
24 and Teuling, A. J.: Investigating soil moisture–climate interactions in a changing climate: A
25 review. *Earth Sci. Rev.*, 99, 125–161, 2010.
- 26 Shukla, J., and Kinter, J. C.: Predictability of seasonal climate variations: A pedagogical
27 review. *Predictability of Weather and Climate*, T. Palmer and R. Hagedorn, Eds., Cambridge
28 University Press, 306–341, 2006.

1 Trenberth, K. E., Branstator, G. W., Karoly, D., Kumar, A., Lau, N.-C., and Ropelewski, C.:
2 Progress during TOGA in understanding and modelling global teleconnections associated
3 with tropical sea surface temperatures. *J. Geophys. Res.*, 103, 14,291-14,324, 1998.

4 Trenberth, K. E., and Dai, A.: Effects of Mount Pinatubo volcanic eruption on the
5 hydrological cycle as an analog of geoengineering. *Geophys. Res. Lett.*, 34, L15702, 2007.

6 Wang, B., and Coauthors: Advance and prospectus of seasonal prediction: Assessment of the
7 APCC/CliPAS 14-model ensemble retrospective seasonal prediction (1980–2004). *Climate*
8 *Dyn.*, 33, 93–117, 2009.

9 Wang, G., Dolman, A. J., and Alessandri, A.: A summer climate regime over Europe
10 modulated by the North Atlantic Oscillation, *Hydrol. Earth Syst. Sci.*, 15, 57-64, 2011a.

11 Wang, G., Sun, S., and Mei, R.: Vegetation dynamics contributes to the multi-decadal
12 variability of precipitation in the Amazon region, *Geophys. Res. Lett.*, 38, L19703, 2011b.

13 Wild, M., Trüssel, B., Ohmura, A., Long, C. N., König-Langlo, G., Dutton, E. G., and
14 Tsvetkov, A.: Global dimming and brightening: An update beyond 2000, *J. Geophys. Res.*,
15 114, D00D13, doi:10.1029/2008JD011382, 2009.

16 Zeng, F.-W., Collatz, G. J., Pinzon, J. E., and Ivanoff, A.: Evaluating and Quantifying the
17 Climate-Driven Interannual Variability in Global Inventory Modeling and Mapping Studies
18 (GIMMS) Normalized Difference Vegetation Index (NDVI3g) at Global Scales, *Remote*
19 *Sens.*, 5, 3918-3950, 2013.

20 Zeng, N., Neelin, J., Lau, W.-M., and Tucker, C.: Enhancement of interdecadal climate
21 variability in the Sahel by vegetation interaction, *Science*, 286, 1537–1540, 1999.

22 Zeng, N., Mariotti, A., and Wetzol, P.: Terrestrial mechanisms of interannual CO₂ variability,
23 *Global Biogeochem. Cycles*, 19, GB1016, doi:10.1029/2004GB002273, 2005.

24 Zhang, K., Kimball, J. S., Nemani, R. R., and Running, S. W.: A continuous satellite-derived
25 global record of land surface evapotranspiration from 1983 to 2006, *Water Resour. Res.*, 46,
26 W09522, doi:10.1029/2009WR008800, 2010.

27 Zhang, J., Wang, W.-C., and Wei, J.: Assessing land-atmosphere coupling using soil moisture
28 from the Global Land Data Assimilation System and observational precipitation, *J. Geophys.*
29 *Res.*, Vol. 113, No. D17119, doi:10.1029/2008JD009807, 2008.

1 Zhu, Z., Bi, J., Pan, Y., Ganguly, S., Anav, A., Xu, L., Samanta, A., Piao, S., Nemani, R. R.,
2 and Myneni, R. B.: Global Data Sets of Vegetation Leaf Area Index (LAI)3g and Fraction of
3 Photosynthetically Active Radiation (FPAR)3g Derived from Global Inventory Modeling and
4 Mapping Studies (GIMMS) Normalized Difference Vegetation Index (NDVI3g) for the
5 Period 1981 to 2011, *Remote Sens.*, 5, 927-948, 2013.

6

1 Table 1. Evapotranspiration (ET) [Zhang et al., 2010], Leaf Area Index (LAI) [Zhu et al.,
2 2013], Soil Moisture (SM) [Liu et al., 2011, 2012], Precipitation (PRE) [Adler et al., 2003]
3 datasets characteristics.

	ET	LAI	SM	PRE
type	satellite	satellite	satellite	gridded from rain gauges
version	-	1.0	0.1	2.2
producer	University of Montana	Boston University	ESA	GPCP
Spatial resolution (original)	1° x 1°	8 km x 8 km	0.25° x 0.25°	2.5° x 2.5°
Spatial resolution (after pre-processing)	1° x 1°	0.5° x 0.5°	0.5° x 0.5°	2.5° x 2.5°
Temporal frequency (original)	monthly	15-days	daily	monthly
Temporal frequency (after pre-processing)	seasonal	seasonal	seasonal	seasonal
units	W m ⁻²	m ² m ⁻²	m ³ m ⁻³	mm d ⁻¹
period	1983-2006	1982-2010	1979-2010	1979-2010

4
5

1 Table 2. Ratios of the global-scale forced and free variance with respect to the total variance
2 resulting from the application of the CM technique between PRE and SM, ET and LAI.

	Forced	Free
SM	0.17	0.83
PRE	0.19	0.81
ET	0.14	0.86
PRE	0.18	0.82
LAI	0.14	0.86
PRE	0.17	0.83

3

4

1 Table 3. PRE variability forced by the SM decomposed through EOF analysis. Each line
 2 displays the EOF explained variance (column 2) and the corresponding PC correlation with
 3 relevant climatic indices (column 3). AOD is the Stratospheric Aerosol Optical Depth.
 4 NINO3 index is defined as the average of the Sea Surface Temperature in the tropical Pacific
 5 region (5° S–5° N, 210–270° E). Here the maximum PC correlation is reported considering
 6 lagged correlations in the range -16 to +16. Only the correlation coefficients significant at 1%
 7 level are reported.

	Variance explained	Correlation with climate indices
PC 1	0.26	0.56 (AOD) at lag 0 (significant in the range: -4/+7)
PC 2	0.14	0.60 (NINO3) at lag 2 (significant in the range: 0/+5)
PC 3	0.08	-
PC >4	<0.07	-

8

9

1 Table 4. Total rainfall variability decomposed through EOF analysis. Each line displays the
 2 EOF explained variance (column 2) and the corresponding PC correlation with relevant
 3 climatic indices (column 3). Here the maximum PC correlation is reported considering lagged
 4 correlations in the range -16 to +16. Only the correlation coefficients significant at 1% level
 5 are reported.

	Variance explained	Correlation with climate indices
PC 1	0.10	0.41 (AOD) at lag 0 (significant in the range: -2/+2)
PC 2	0.05	0.43 (NINO3) at lag 2 (significant in the range: +1/+4)
PC >3	<0.04	-

6
7

1 Table 5. Ratios of the global-scale forced and free variance with respect to the total variance
2 resulting from the application of the CM technique between PRE forced by SM and ET, LAI.

	Forced	Free
PRE forced by SM (forced by ET)	0.20	0.80
PRE forced by SM (forced by LAI)	0.23	0.77

3

1 Table 6. Ratios of the global-scale forced variance over the total variance resulting from the
2 application of the CM technique between the first three modes of PRE forced by SM and the
3 total fields of ET and LAI.

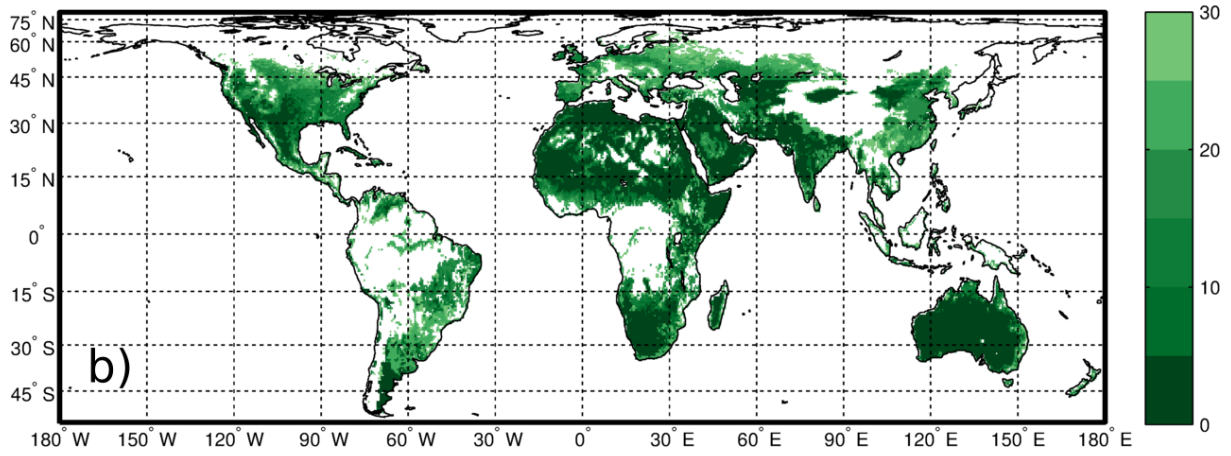
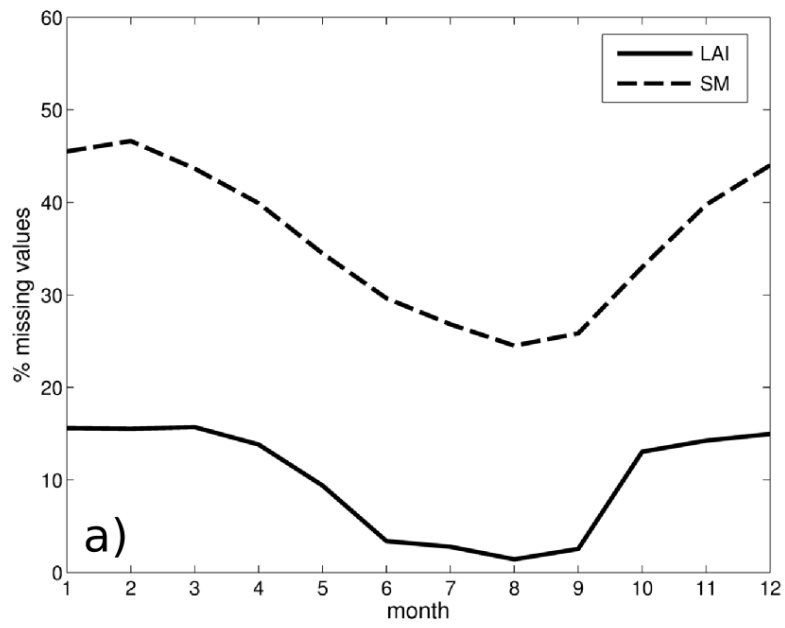
	ET	LAI
PRE forced by SM mode 1	0.21	0.27
PRE forced by SM mode 2	0.38	0.36
PRE forced by SM mode 3	0.31	0.29

4

1 Table 7. Rainfall variability forced by the ET and LAI decomposed through EOF analysis.
 2 Each line displays the EOF explained variance (column 2) and the corresponding PC
 3 correlation with relevant climatic indices (column 3). Here the maximum PC correlation is
 4 reported considering lagged correlations in the range -16 to +16. Only the correlation
 5 coefficients significant at 1% level are reported.

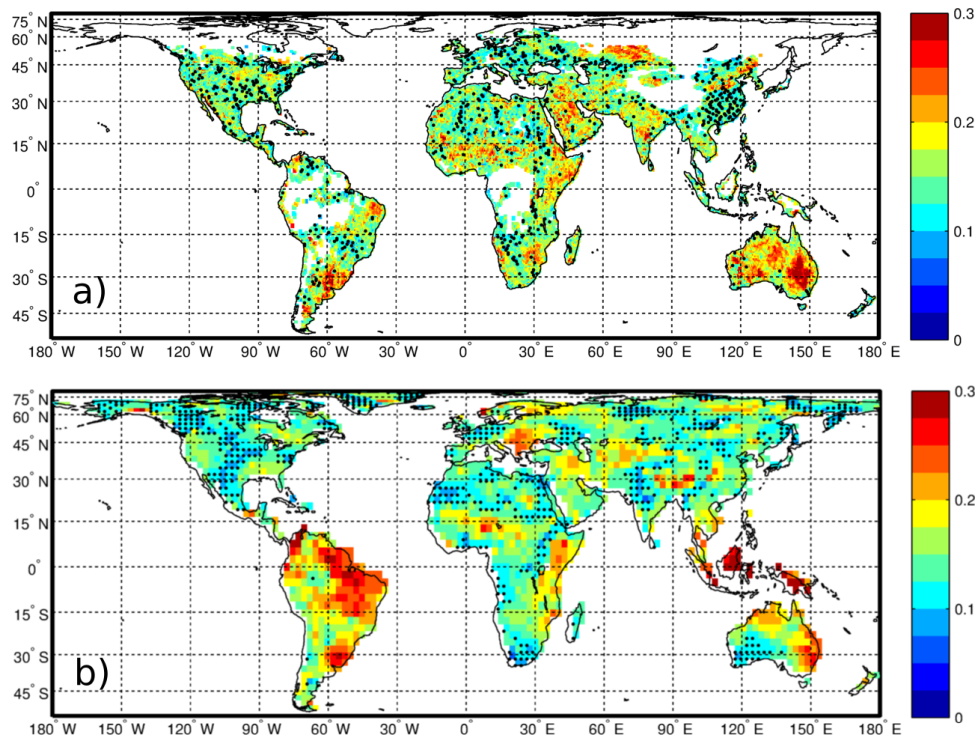
	Variance explained	Correlation with climate indices
PRE forced by ET		
PC 1	0.30	0.52 (NINO3) at lag 0 (significant in the range: -2/+2)
PC 2	0.13	-
PC 3	0.07	0.41 (AOD) at lag 6 (significant in the range: +3/+10)
PC >4	<0.05	-
PRE forced by LAI		
PC 1	0.27	0.67 (NINO3) at lag 0 (significant in the range: -2/+2)
PC 2	0.10	0.41 (AOD) at lag 3 (significant in the range: 0/+5)
PC 3	0.09	-
PC >4	<0.06	-

6



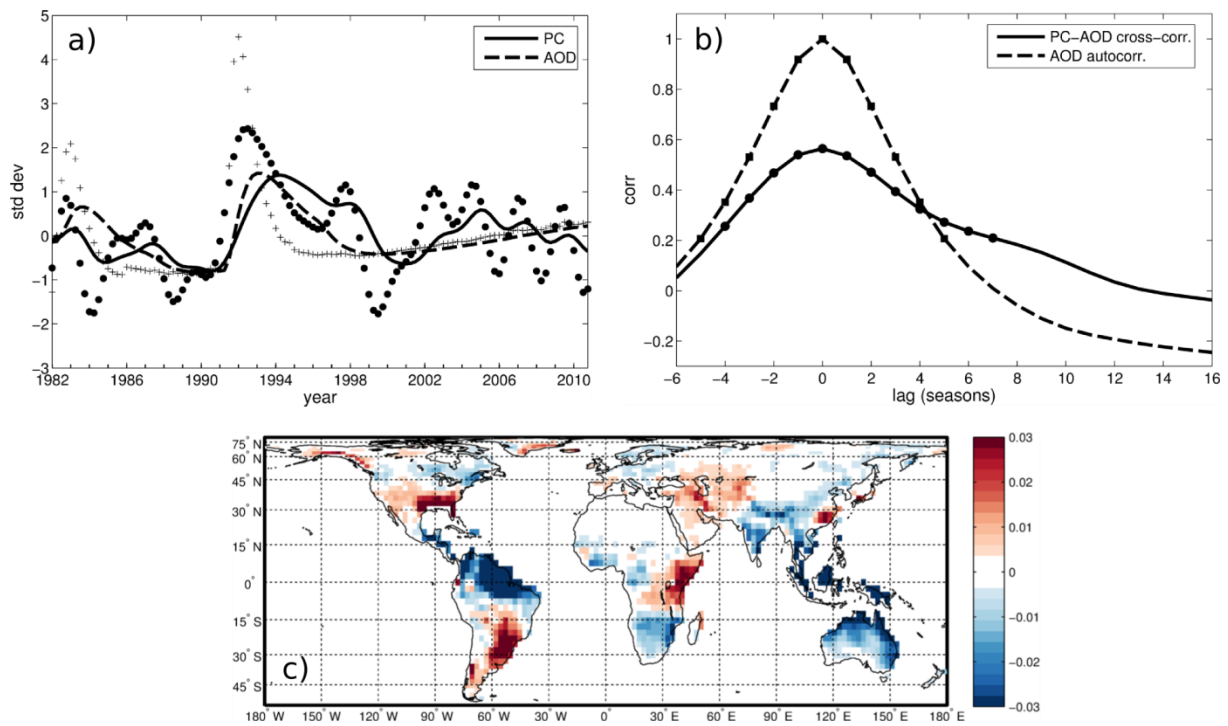
1
2
3
4
5

Figure 1. (a) Global mean missing values in the time series (in %): LAI (full), SM (dashed).
(b) Map of the percentage of SM missing data for each grid point.



1
2
3
4
5
6
7

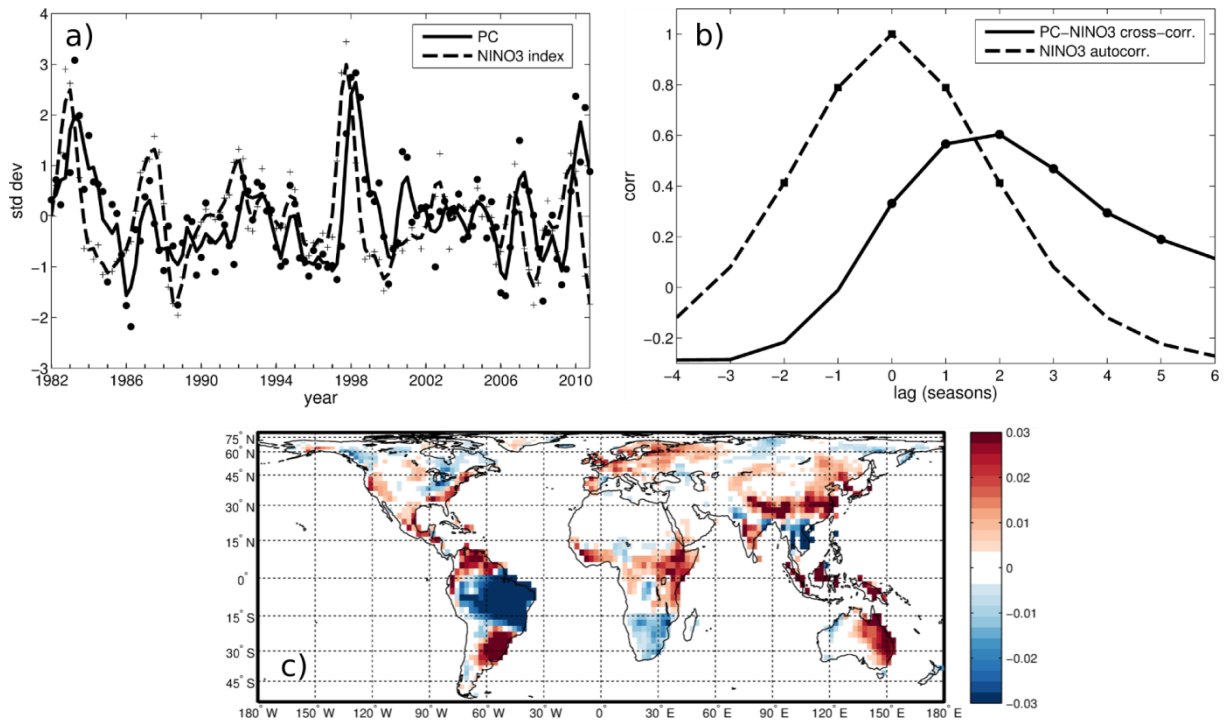
Figure 2. Ratio of the forced variance to the total variance. (a) The fraction of SM variance forced by PRE. (b) The fraction of PRE variance forced by the SM. Dots are placed over areas covered by the forced variable dataset but where variance ratio values did not pass a significance test at the 1% level.



1

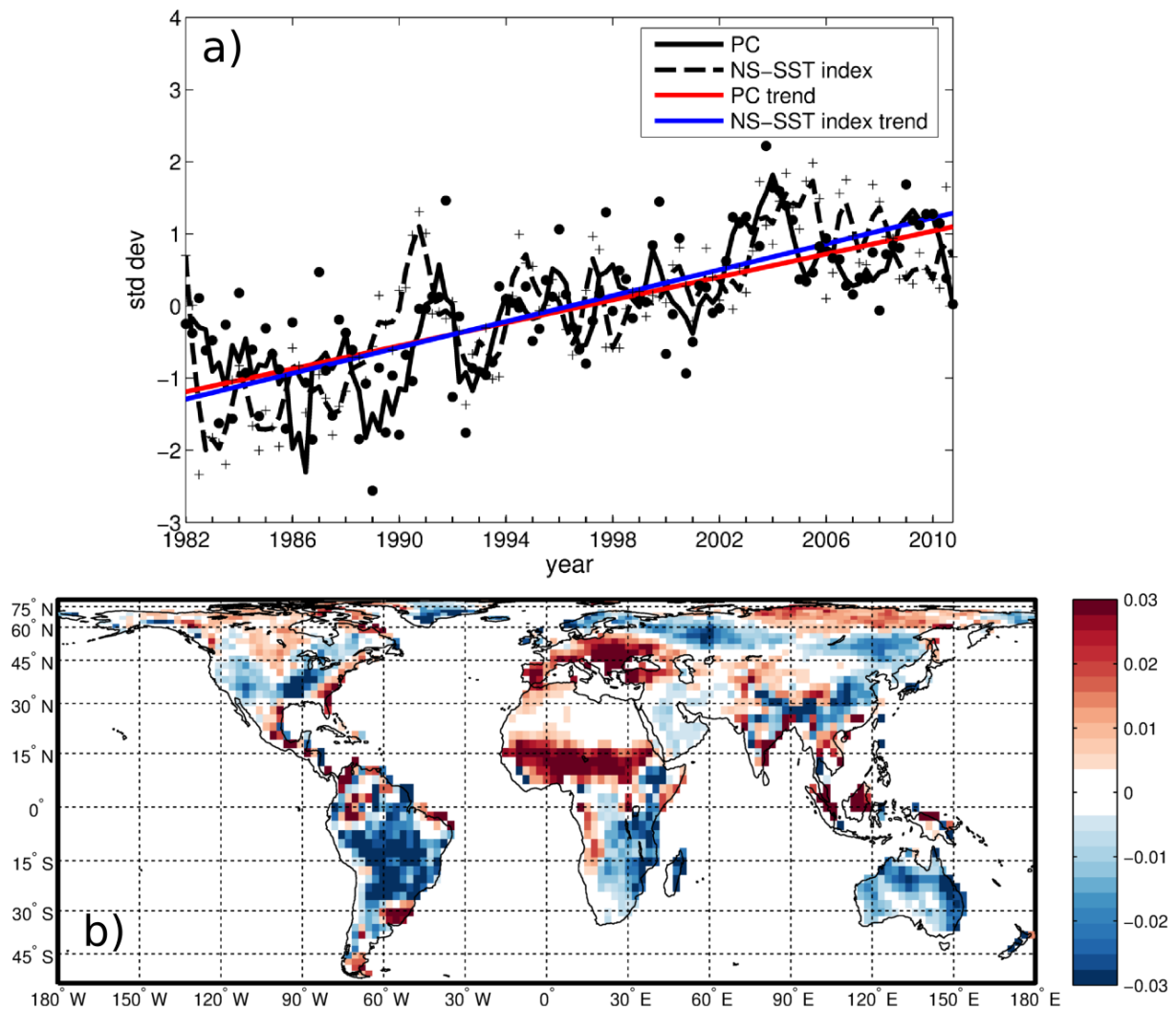
2

3 Figure 3. (a) First normalized PC of the PRE anomalies forced by the SM (full line and filled
 4 circles), after cutoff low-pass filtering at 2 year-1 frequency. Dashed line (and cross marks)
 5 stands for the normalized stratospheric Aerosol Optical Depth (AOD). Lines stand for 5-years
 6 exponential moving average while marks represent each single season. (b) Lagged
 7 correlations between AOD and PC1 of the forced PRE. The dashed curve is the
 8 autocorrelation function of the AOD. Marks indicate significance at the 5% level. (c) First
 9 EOF of the forced PRE. Arbitrary units.



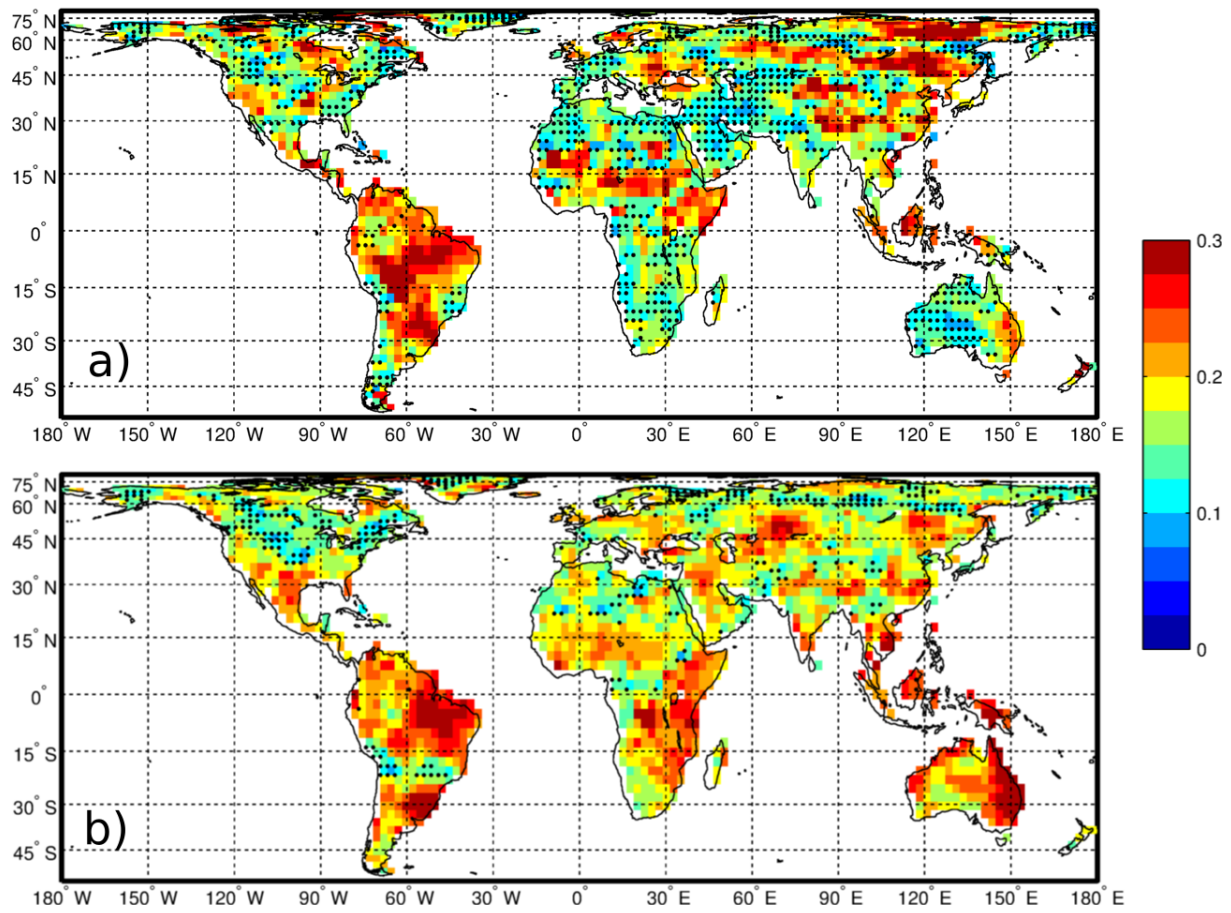
1
2
3
4
5
6
7
8
9

Figure 4. (a) Second normalized PC of the PRE anomalies forced by the SM (full line and filled circles). Dashed line (and cross marks) stands for the normalized NINO3 index. Lines stand for 3-seasons running means while marks represent each single season. (b) Lagged correlations between NINO3 index and PC1 of forced PRE. The dashed curve is the autocorrelation function of the NINO3 index. Marks indicate significance at the 5% level. (c) Second EOF of the forced PRE. Arbitrary units.



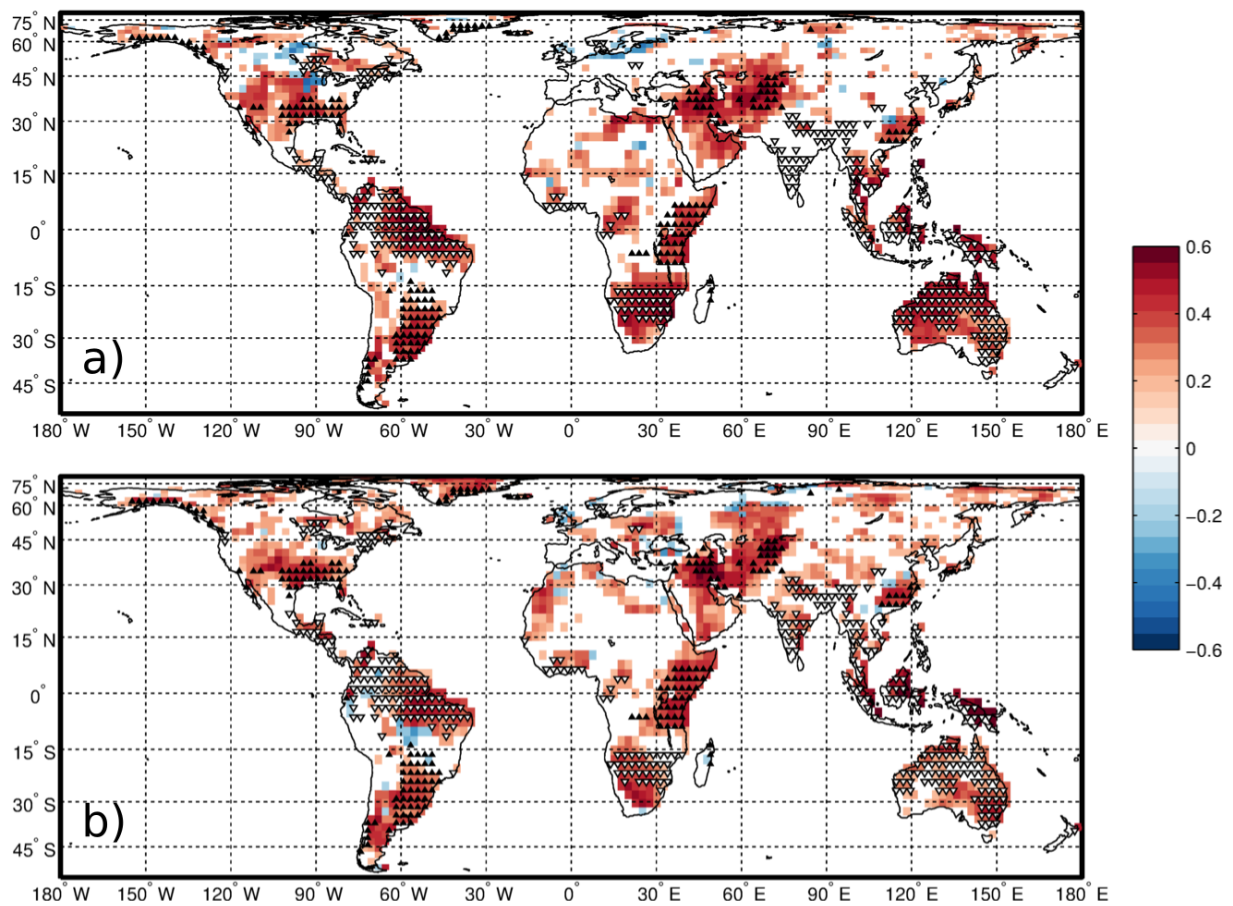
1
2
3
4
5
6
7
8

Figure 5. (a) Third normalized PC of the PRE anomalies forced by the SM (full line and filled circles). Dashed line (and cross marks) stands for the normalized NS-SST index. Lines stand for 3-seasons running means while marks represent each single season. Coloured lines represent the trends (red for the PC, blue for the NS-SST index). (b) Third EOF of the forced PRE . Arbitrary units.



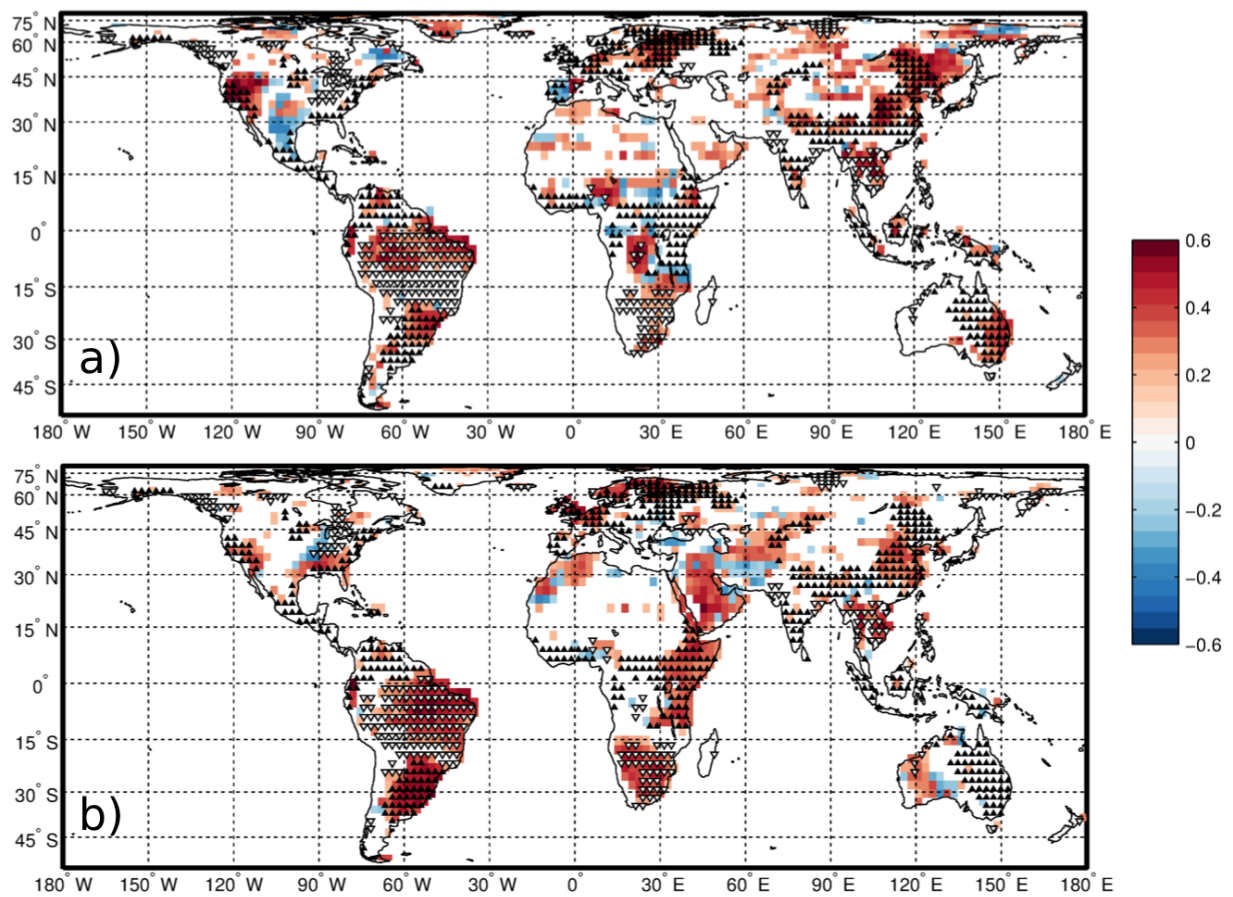
1
2
3
4
5
6
7

Figure 6. Ratio of the forced variance to the total variance. (a) The fraction of PRE variance forced by the SM which is also forced by the ET. (b) The fraction of PRE variance forced by the SM which is also forced by the LAI. Dots are placed over areas where variance ratio values did not pass a significance test at the 1% level.



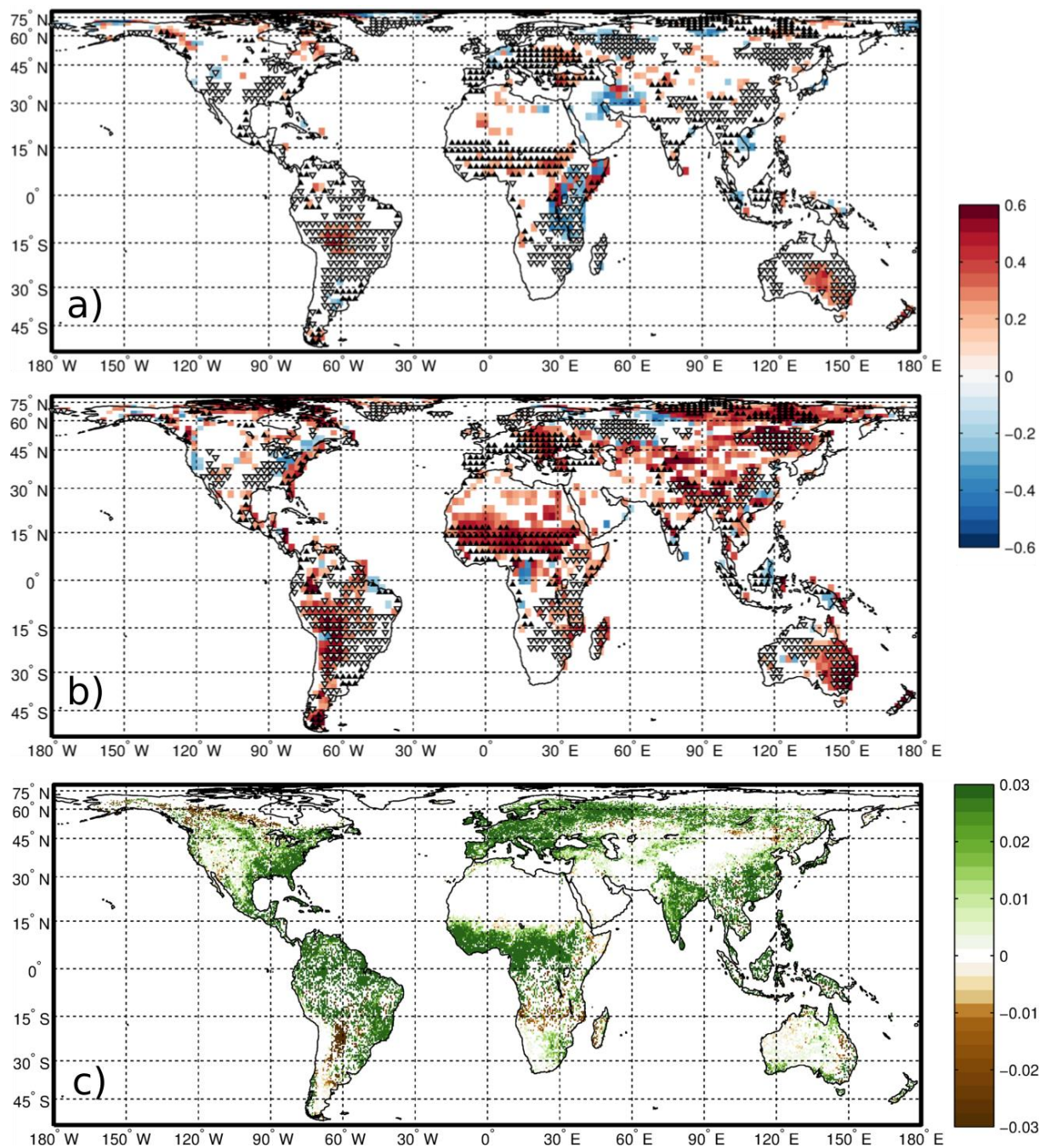
1
2
3
4
5
6
7
8
9

Figure 7. Point-by-point correlation of the first mode of variability of PRE forced by SM with (a) the total fields of PRE forced by ET and (b) the PRE forced by LAI. Data have been filtered using a cutoff low-pass filter at 1 year frequency. Only areas where correlations passed a significance test at the 5% level are shown. Black upward (white downward) triangles denote areas with positive >0.01 (negative <-0.01) values of the first EOF of the PRE anomalies forced by the SM (Fig. 3c).



1
2
3
4
5
6
7
8
9

Figure 8. Point-by-point correlation of the second mode of variability of PRE forced by SM with (a) the total fields of PRE forced by ET and (b) the PRE forced by LAI. Data have been filtered using a cutoff low-pass filter at 1 year frequency. Only areas where correlations passed a significance test at the 5% level are shown. Black upward (white downward) triangles denote areas with positive >0.01 (negative <-0.01) values of the second EOF of the PRE anomalies forced by the SM (Fig. 4c).



1

2

3 Figure 9. Point-by-point correlation of the third mode of variability of PRE forced by SM on
 4 the total field of (a) PRE forced by ET and (b) PRE forced by LAI. (c) Magnitude of the LAI
 5 change over 1982-2010, quantified using a linear model under the assumption of monotonic
 6 change. Data have been filtered using a cutoff low-pass filter at 1 year⁻¹ frequency. Only
 7 areas where correlations (panels a-b) and trend (panel c) passed a significance test at the 5%
 8 level are shown. Black upward (white downward) triangles denote areas with positive >0.01
 9 (negative <-0.01) values of the third EOF of the PRE anomalies forced by the SM (Fig. 5b).